Anode region design and focusing properties of STAR Silicon Drift Detectors

R.Bellwied [d], R.Beuttenmuller [a], W.Chen [a], D.DiMassimo [a], L.Dou [d], H.Dyke [b], A.French [d], J.R.Hall [d], G.W.Hoffmann [c], T.J.Humanic [b], I.V.Kotov [b,e,1], H.W.Kraner [a], Z.Li [a], C.J.Liaw [a], J.Lopez [b], D.Lynn [a], V.L.Rykov [d], S.U.Pandey [d], C.Pruneau [d], J.Schambach [c], J.Sedlmeir [a], E.Sugarbaker [b], J.Takahashi [d,f], W.K.Wilson [d]

Accepted for publication in Nucl. Instr. Meth.

STAR–SVT Collaboration

[a] *Brookhaven National Laboratory, Upton, NY 11973, USA*

[b] *The Ohio State University, Columbus, OH 43210, USA*

[c] *University of Texas, Austin, TX 78712, USA*

[d] *Wayne State University, Detroit, MI 48201, USA*

[e] *IHEP, RU–148284 Protvino, Moscow region, Russia*

[f] *University of Sao Paulo, Brasil*

Electron collection at the anodes of large–area silicon drift detectors was studied with STAR2 prototypes. Results of measurements of anode leakage currents, signal dependence on focusing voltages, anode uniformity, and model simulations are reported. A design of the anode region is presented. The design optimization is discussed.

Introduction

This article presents the design and reports on the performance properties of the anode region of Silicon Drift Detectors (SDD's) for the Silicon Vertex

[1] Corresponding author. Phone: (614)–292–4775; fax: (614)–292–4833; e–mail: kotov@mps.ohio-state.edu

Tracker (SVT) of the RHIC STAR experiment [1]. The SVT will consist of 216 SDD's. Prototype detectors with bi–directional drift and total area 6.3×6.3 cm^2, of which 94% is active, were built and tested. The drift length is 30 mm each way from the central high voltage strip. The drift regions end at a row of 239 anodes on each of the two opposite edges of the detector. A schematic view of the anode region is shown in fig.1. Further details about STAR SDD's can be found in [2].

The general principles of operation of SDD's are discussed elsewhere [3,4]. In the SDD fabricated on n–type silicon the electrons created by an ionizing particle drift toward the anodes. In the main part of the detector an electron cloud drifts in the middle of the bulk, where the electric potential is rather insensitive to Si–SiO_2 interface conditions. The biasing of electrodes near the anodes controls the collection of the electron cloud onto the anodes, which reside on the surface. Approaching the surface, the electron cloud enters a region where surface conditions play an important role. The electric potential in that region should be optimized to provide good focusing and charge collection.

Two detector designs, STAR2.7 and STAR2.8, are discussed in this paper. Section 1 briefly describes the design of the anode region. In sections 2–4 simulation and test results are presented. We conclude with a summary of the anode performance.

1 Design and processing

The SVT detectors have an anode lateral pitch of 250 μm. Anodes are located on the n–side of the wafer and separated from each other by an E1 p^+ electrode and silicon oxide (see fig.1). Under the anodes and E1 a p^+ electrode called W1 is placed on the opposite side (p–side) of the wafer (see fig.1) to deflect the drifting electrons to the anode. The cathode strip structure (see [2]) is identical on both n– and p–sides. External biasing can be applied to each fifth cathode. Cathodes in the focusing region (N0, N5, N10, N15 on n-side and P0, P5, P10, P15 on p–side) can be biased independently to provide fine tuning of the focusing field. Starting from cathode 20, the biasing is the same on both sides.

There were built and tested 43 STAR2.7 detectors and 6 STAR2.8 detectors. The detectors were fabricated on 4 in. diameter, 280μm thick, n-type, 3.5 kΩ cm NTD wafers with (111) crystal orientation. They were produced by the planar process technique in the silicon laboratories at BNL and SINTEF (Norway).

A phosphorus (n^+) implant was performed to produce the anode read out

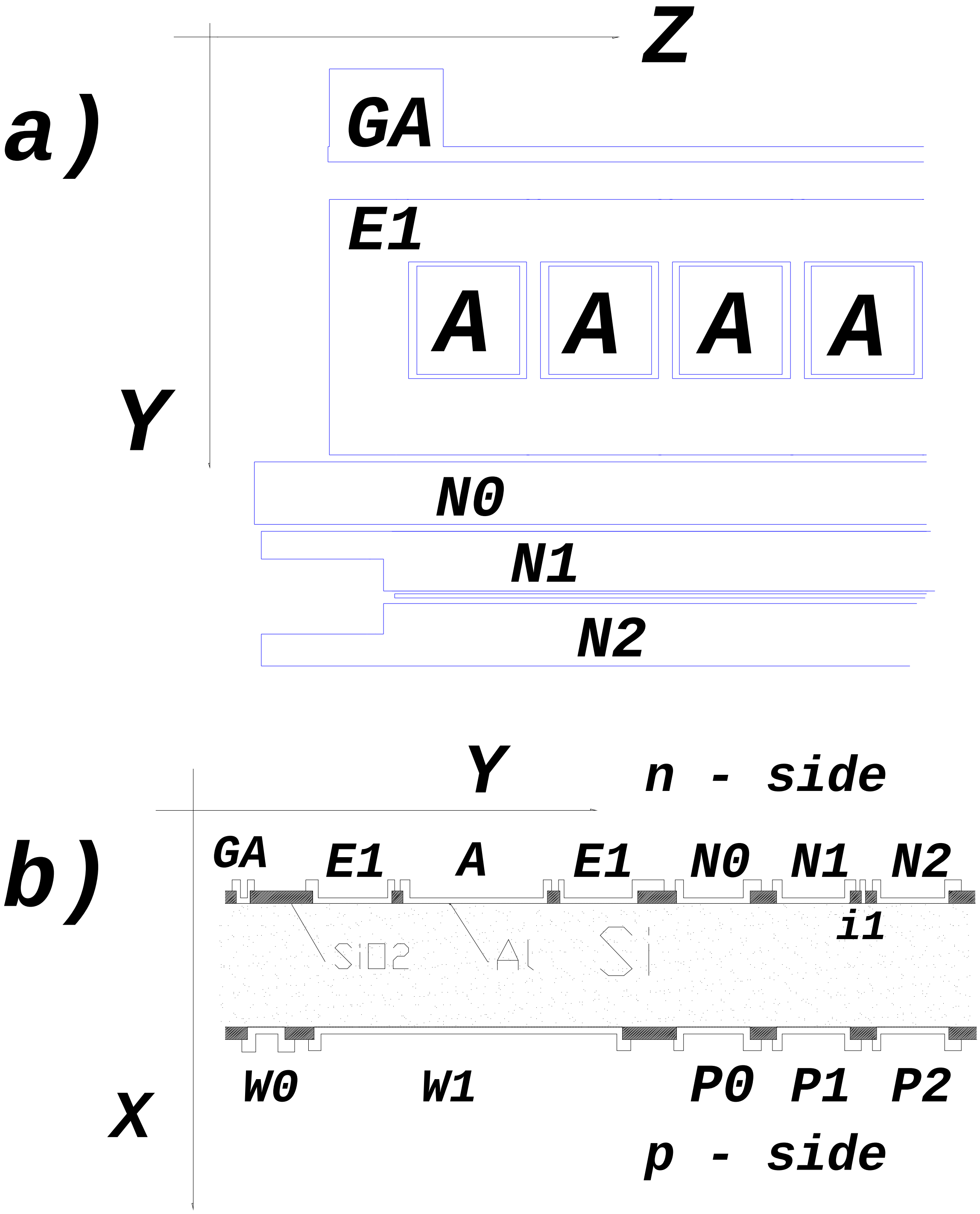

Fig. 1. Schematic view of the anode region of the STAR2.8 detector: a) AutoCad drawing of the n–side aluminum mask; b) detector cross–section along drift direction; GA — guard anode; A — readout anode; N0, N1, N2 — cathodes on the n–side; P0, P1, P2 — cathodes on the p–side; E1, W1 — focusing electrodes; W0 — guard electrode on the p–side; i1 — injector #1. Axis definition: Z — along anodes; Y — parallel to drift direction; X — perpendicular to the detector surface.

contacts. The implant dose was both $1 \times 10^{13}/cm^2$ at 40 keV and $1 \times 10^{13}/cm^2$ at 65 keV through 1000Å of SiO_2. The dimensions of this n^+ implantation are 206×196 μm in the STAR2.7 design and 188×196 μm in STAR2.8. Anode pads are separated from each other by a 21 μm strip of the p^+ implant (see fig.1 for details). Gaps between n^+ and p^+ implants are 11.5 μm on STAR2.7 and 20.5 μm on STAR2.8. One can consider the anode–E1 structure as a diode. This diode is normally reverse biased. Maintaining a low level of the reverse current is important because this current contributes to the anode leakage current. A high value of the reverse breakdown voltage is also important for better focusing. For these reasons, it is easier to produce good and reliable structures with wider anode–E1 gap.

An implant of boron (p^+) was also performed to produce p^+n rectifying junctions. The dose was $1.15 \times 10^{13}/cm^2$ at 45 keV. There are 441 p^+ cathode strips on each surface. The strip width is 100 μm with a pitch of 135 μm. The degree of metalization overlay was optimized by simulation. Cathodes are connected by implanted 500 kΩ resistors between cathode strips. The width of the W1 strip is 387 μm on STAR2.7 and 420 μm on STAR2.8.

The main differences between the STAR2.7 and 2.8 designs in the anode region are: the STAR2.8 has a wider anode–E1 gap and narrower E1–N0 and W1-P0 gaps. The effect of the geometry of the focusing electrodes is discussed below.

2 Simulation of the electric potential in the anode region

The simulated negative electric potential within the detector close to the readout anode is shown in fig.2. The differential equation for the electric potential was solved numerically on a grid composed of $5\mu m \times 5\mu m$ cells. Each cell is allowed to be either fully depleted or completely undepleted. The effects of the surface charge were not considered. The biasing used is close to the optimum conditions determined experimentally. The electric potentials on both the n–side and the p–side exhibit a step shape which approaches the designed smooth fall–off to the readout anodes as one goes deeper into the bulk. The bottom of the potential valley is located approximately in the middle of the detector and goes linearly down to the anode, which is set at zero potential. The readout anodes are separated from the guard anode by a potential barrier of about 8 volts created by an over–depletion between E1 and W1. For the bulk region of the detector the results of these calculations are in substantial agreement with more complete calculations described below.

To take into account the interface states density, we used the SILVACO simulation package [5]. A typical value of the interface states density N_{it} for our standard detector processing at BNL is about $2 \times 10^{11} cm^{-2}$. If the detector is

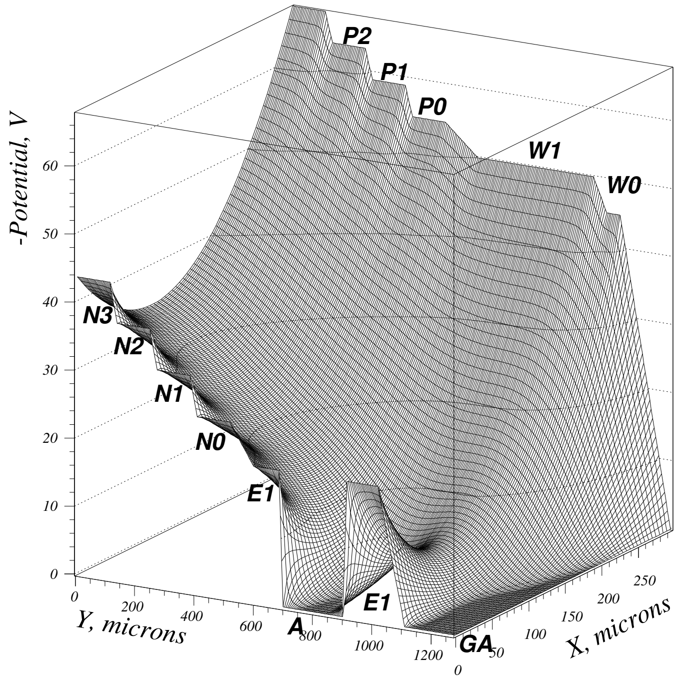

Fig. 2. Negative electric potential in the anode region for silicon resistivity of 4 kΩcm. Location of some electrodes are marked: N0, N1, N2, N3 — cathodes on the n–side; P0, P1, P2 — cathodes on the p–side; A — anode; E1, W1, W0 and GA are also shown.

subjected to ionizing radiation, N_{it} also increases [6,7]. This interface charge is normally positive and it causes an accumulation of electrons in the silicon beneath the SiO_2. As a result such regions (the area on fig.1 between the cathodes and between E1–N0 and W1–P0) are difficult to deplete and under some circumstances potential wells could become electron traps.

Fig.3a shows the electric potential calculated for the STAR2.7 structure assuming an interface states density of $2 \times 10^{11} cm^{-2}$. The bias assignment for fig.3 was chosen to emphasize the effect of wells and is listed in Table 1. The potential wells for electrons are clearly seen between the cathodes. Two deep wells between cathode N0 and E1 (well B) and cathode P0 and W1 (well C) are particularly visible. The well B can be a substantial trap for drifting electrons since it precedes the readout anode along the drift path.

The effect of well B can be reduced by changing the spacing between N0 and E1. In STAR2.8 the effective gaps N0–E1 and P0–W1 are reduced from those in STAR2.7 by two means: the reduction of the SiO_2 width (W_{ox}) between electrodes and the reduction of the gap between the Al field plates (Gap_{Al}). Table 2 summarizes the major changes between STAR2.8 and STAR2.7.

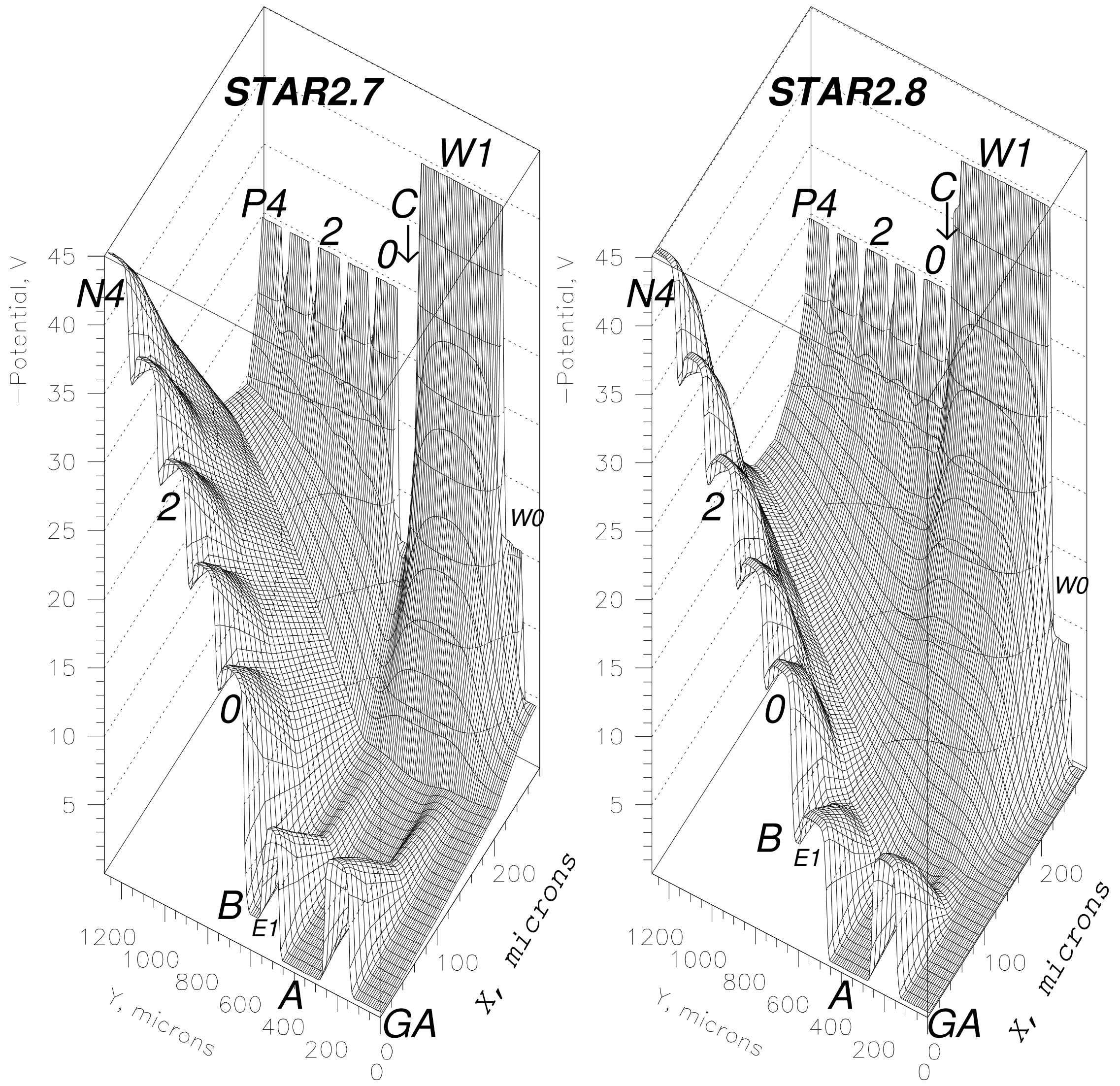

Fig. 3. Negative electric potential with an interface states density $2 \times 10^{11} cm^{-2}$ for a) STAR2.7, b) STAR2.8 structures. Location of wells B and C and some electrodes are marked: N0, N2, N4 — cathodes on the n–side; P0, P2, P4 — cathodes on the p–side; A — anode; E1, W1, W0 and GA are also shown.

Fig.3b shows the calculated electric potential near the anode region for the STAR2.8 structure with the same assumptions. Profiles of the electric potential along a cut line going through gaps W1–P0 and E1–N0 from well B to well C for STAR2.7 and STAR2.8 are shown in fig.4. The central valley in the potential profile is well defined for STAR2.8 and is shallow for STAR2.7. The

Table 1
Biasing assignment (in volts) on the electrodes for the calculations shown in fig.3.

p-side	W0	W1	P0	P1	P2	P3	P4	
	float	-40	-30	-30	-30	-30	-30	
n-side	GA	Anode	E1	N0	N1	N2	N3	N4
	0	0	-10	-20	-26.5	-33	-39.5	-46

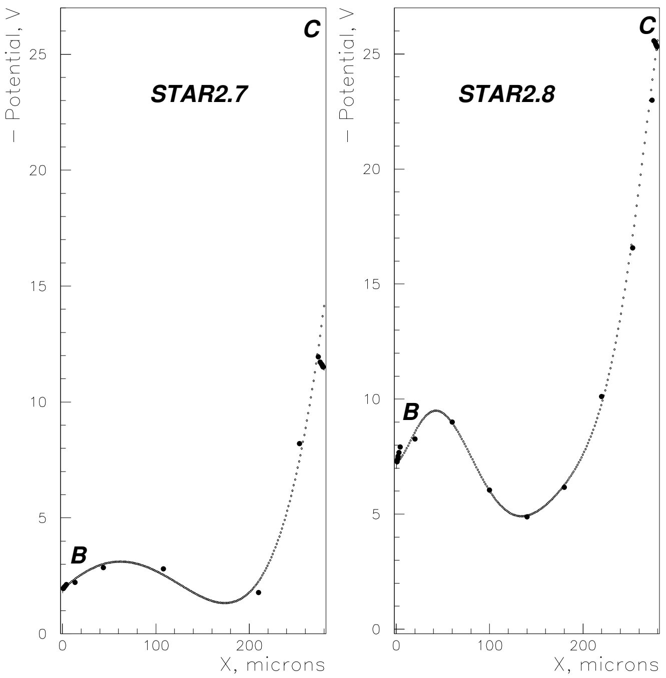

Fig. 4. Negative electric potential along a cut line going through gaps W1–P0 (well B) and E1–N0 (well C). Smooth lines are polynomial fit. Position of wells B and C are shown.

Table 2
Changes between STAR2.7 and 2.8 design.

	W1–P0 gap (μm)		E1–N0 gap (μm)	
	W_{ox}	Gap_{Al}	W_{ox}	Gap_{Al}
STAR2.7	101	94	104	82
STAR2.8	74	31	53	17

depth of both potential wells B and C are significantly reduced by these geometry improvements in the STAR2.8 structure. The drift channel for electrons clearly leads to the readout anode.

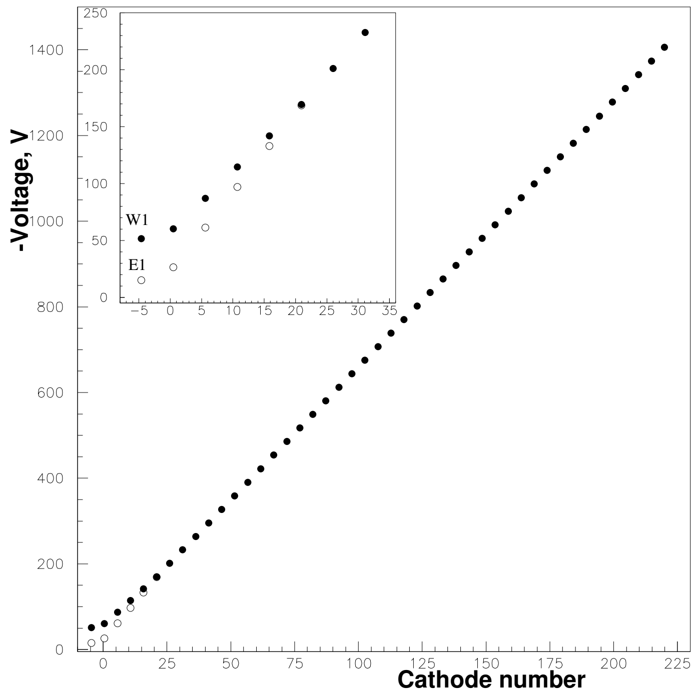

Fig. 5. Voltage distribution measured on the STAR2.7 detector S15. Open circles — for n–side cathodes, black dots — for p–side; two left points — E1,W1 voltages. The insert shows the focusing region.

The biasing also affects the potential distribution in the anode region. According to simulations one biasing strategy might be the following: put the same biases on n– and p–sides to keep drifting electrons in the middle of the bulk and as far away from electron traps as possible. Full depletion of the region under the anodes occurs at W1≈-80V, if E1 is close to 0V. The combined action of E1 and W1 depletes that region at W1≈-50V, E1≈-15V to -20V (see fig.7), and it is not practical to use much higher E1 voltage due to approaching the breakdown. It is therefore not possible to maintain equality of biasing on the n– and p–sides near the anodes. Other considerations such as requirements of good linearity over the total drift distance also affect the choice of biasing.

3 Biasing

Cathode strip potentials are defined by periodic connections (each 5-th cathode for the present study) to an external voltage divider. The example of a voltage distribution across cathodes is shown in fig.5. In the regular drift region (between cathodes 20 and 221) a linearly increasing negative potential was applied to junctions. In the focusing region (cathodes 0 – 20) different

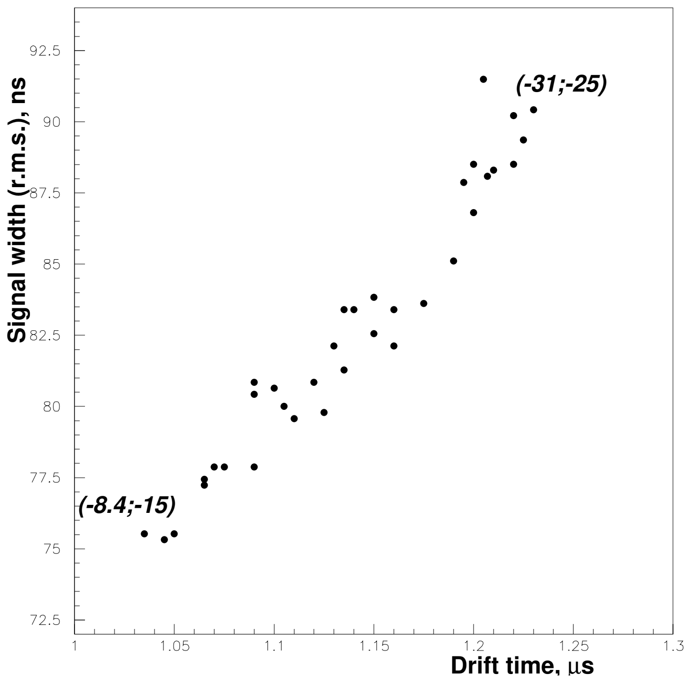

Fig. 6. Drift time — signal width correlation measured in a STAR2.8 detector in laser tests for various trajectories. Different trajectories were generated using various E1, N0 values. The (E1;N0) voltages in volts are shown for minimum and maximum drift time.

approaches were tested. The correlation between the drift time of the laser generated electron cloud and the output signal width measured during the laser bench tests (see section 4 for details) is shown in fig.6. The voltage distribution on the p–side was the same as shown in fig.5. Voltages on E1 and N0 were varied and the voltage distribution between N0 and cathode 20 was adjusted to remain linear. The laser spot was located just beyond the focusing region at a distance of 3 mm from the anode. The biasing voltage of cathode 20 was fixed, therefore all changes in the drift time are due to changes in the electron trajectories, however for each trajectory the same number of electrons were collected on the readout anode.

As seen from fig.6 the fastest trajectory gives the smaller signal width. One of the voltage settings which gives a straight trajectory is a linear voltage distribution on both sides with the slopes controlled by the E1 potential on the n–side and the W1 potential on the p–side. The results presented below were obtained using this type of biasing, although it is possible to shrink the focusing region down to E1 and W1 electrodes.

The range of acceptable E1 voltages is limited by the breakdown voltage of the anode–E1 junctions. The range of acceptable W1 voltages is also limited. At high values of the W1 voltage it is not possible to focus electrons onto the anode because the electron cloud is pushed onto the n–side surface before arriving at the anode. At low values of W1 and E1 voltages the region under the anodes is not depleted and readout anodes are not electrically isolated from each other and from the guard anode. In the SVT, biasing of the detectors will be daisy–chained. It is therefore necessary to have common regions of biasing for all detectors on a ladder.

4 Test results

For testing purposes detectors were bonded to motherboards with hybrid preamplifiers [8]. The width of the response of the electronics for an input delta function is 45 ns. The data were read out via 500 MHz digital oscilloscope TDS640A. For voltage and current measurements, a Keithley 617 electrometer and Keithley 485 picoammeters were used, respectively.

Simple measurements were carried out to determine at which E1 and W1 voltage settings the anode region of the detector is depleted. A small voltage difference, for example 0.1V, is applied between two neighboring anodes and the current is measured as a function of E1 and W1. The conductance between neighboring anodes for the STAR2.7 detector S15 is shown in fig.7. At full depletion the channel between anodes is closed and the conductance value becomes very low.

The anode leakage current measurements for 120 consecutive anodes on the STAR2.8 detector # 652 showed that all currents are less than 100 nA and a typical value is about 0.5 nA. The equivalent noise charge (ENC) of the shot noise of this current is proportional to $\sqrt{I_{leak} \cdot \sigma}$, where σ is the width of the preamplifier–shaper response function. For SVT preamplifier–shapers and $I_{leak} = 0.5$ nA, $ENC_{leak} = 20e$ and is well below SVT requirements.

Uniformity in the response of anodes to charge injection through E1 was measured. There is a capacitive coupling between anodes and E1. The value of the capacitance depends on the geometry and the capacitance of the reverse biased anode–E1 junction. The values of the injected signal amplitudes for 120 anodes in a row of a STAR2.7 detector are shown in fig.8. The variation of the amplitudes is about 3% for most of the anodes. A few anodes show a drastically different response, which is correlated with high level of leakage currents on these anodes.

The potential distribution in the anode region is determined mainly by the voltages applied to E1 and W1. Therefore we measured the amplitude and

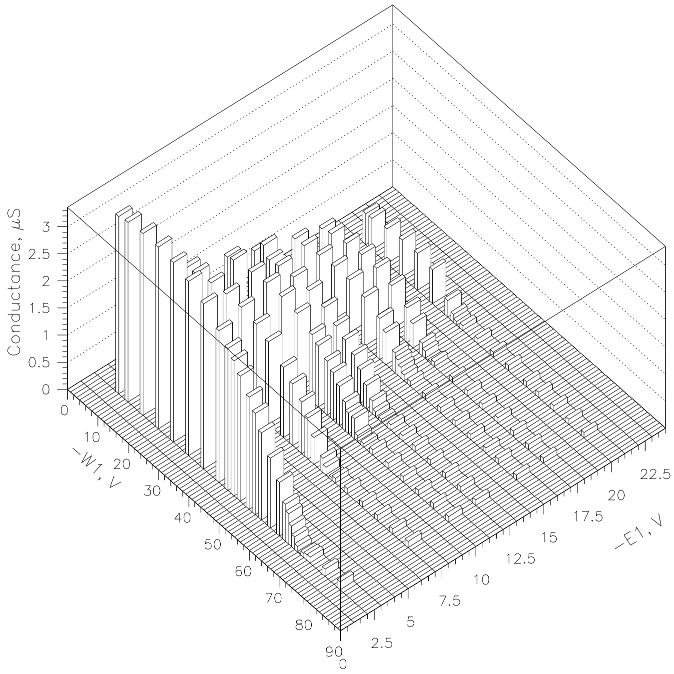

Fig. 7. Dependence of the conductance between neighboring anodes on E1 and W1 voltages.

width of the signal generated by a Nd:YAG laser as well as leakage currents on different anodes of several detectors at different E1 and W1 voltages. The results over a broad E1–W1 space obtained with a STAR2.8 detector are shown in fig.9. Since we have seen breakdown at E1 voltages of about -40V with STAR2.7 detectors, we kept the E1 voltage below this value for the tests reported here.

According to our measurements, the electron cloud can be collected on the readout anodes in a broad range of focusing voltage settings. One should however seek an operational point where signal amplitude is maximum although stable under minor changes of operational conditions. The signal pulse width and the anode leakage current should be minimal to get optimum position resolution from the detector. Optimal focusing voltages are found to be in the vicinity of E1$\simeq$-20V and W1$\simeq$-45V to -50V. At these settings the anode region is fully depleted. In fig.9 the signal is seen at less negative E1 and W1 voltages, which indicates that detectors can operate with a partially depleted anode region. We did not see any signal when W1 was more negative than -80V. The acceptable region of E1, W1 voltages for STAR2.7 detectors is smaller compared to STAR2.8, which could be a result of improvements in the STAR2.8 design such as smaller E1–N0 and W1–P0 gaps.

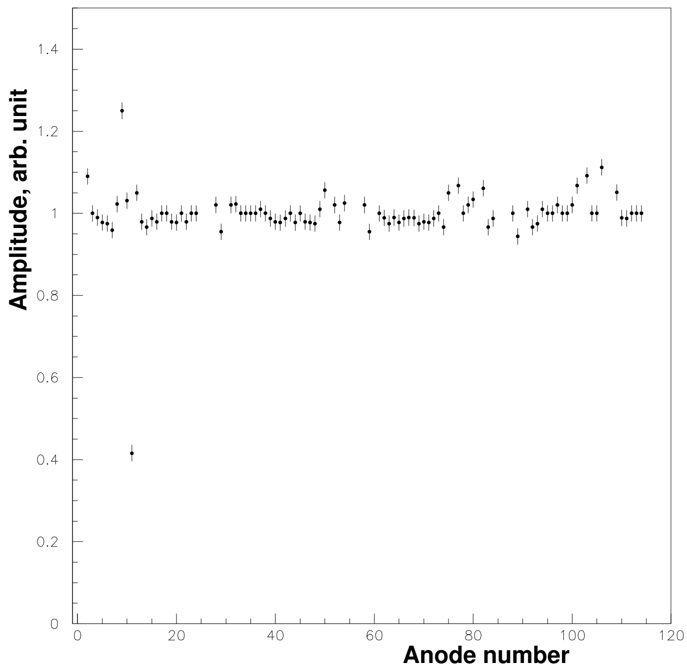

Fig. 8. Signal amplitudes from different anodes in response on E1 pulsing.

5 Summary

The performance of the two SDD designs is reported. The shape of the electric potential in the anode region was studied using 2D simulation packages. Possible electron traps (wells B and C) in the anode region of the STAR2.7 design were evidenced by simulation and shown to be greatly reduced by the geometry changes made for STAR2.8. These changes produced a device with larger effective readout E1–W1 space, thus better assuring the compatibility of several devices biased by a common identical voltage distribution.

We studied the effect of different operating biases of electrodes in the anode region on the signal parameters and anode leakage currents. A low level of the anode leakage currents is achieved. The anode to anode signal read out is found to be uniform within 3% when the detector is pulsed on the E1 electrode. We have found that good charge collection can be achieved over a broad range of focusing voltage settings. Optimal focusing occurs at a fully depleted anode region although detectors can operate when the anode region is partially depleted.

We have established a robust design (STAR2.8) of the anode region of the SDDs being built for the STAR experiment at RHIC.

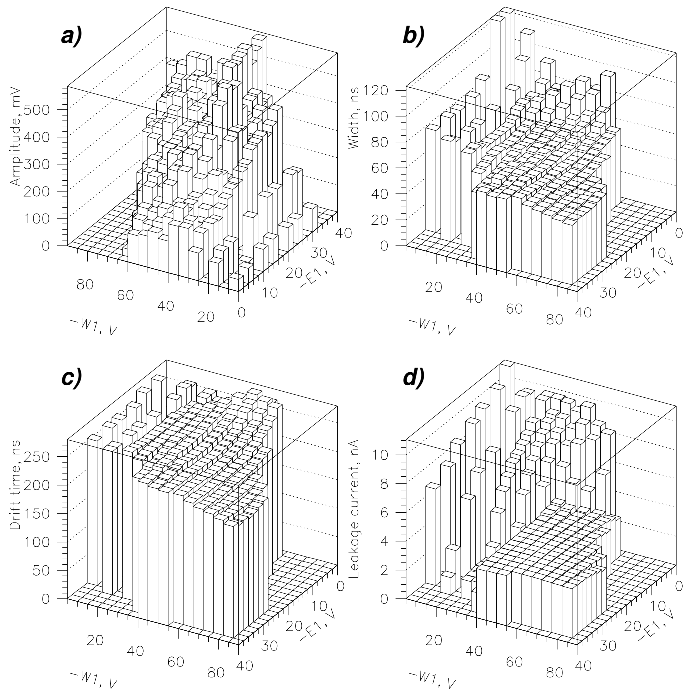

Fig. 9. Dependence of a) signal amplitude, b) width, c) drift time and d) anode leakage current on E1 and W1 setting.

6 Acknowledgments

This work was supported in part by the US Department of Energy grants DE–AC02–76CH00016 and DE–FG03–94ER–40485, NSF grant PHY–9511850, STAR R&D funds and Robert A. Welch Foundation.

References

[1] J.W.Harris and the STAR collaboration. *Nucl. Phys.* **A566** (1994) 277c–286c.

[2] R.Bellwied *et al.*, STAR SVT Group, *Nucl. Inst. and Meth.,* **A377** (1996) 387–392.

[3] E.Gatti and P. Rehak, *Nucl. Inst. and Meth.* **225** (1984) 608.

[4] P.Rehak *et al.*, *Nucl. Inst. and Meth.* **A235** (1985) 224–234.

[5] SILVACO International. 2D Device simulation framework.

[6] S.U.Pandey *et. al.*, *Nucl. Inst. and Meth.* **A361** (1995) 457–460.

[7] H.W.Kraner *et.al.*, Italian Physical Soc. Conf. Proc., Vol. 46, p.141 (1994); *Large Scale Application and Radiation Hardness of Semiconductor Detectors, A.Baldini & E.Forcardi, eds., SIF, Bologna.*

[8] Veljko Radeka, Low–noise techniques in detectors, *Ann. Rev. Nucl. Part. Sci.* 1988, 38 p.217–277.